Integrated nanotechnology platform for tumor-targeted multimodal imaging and therapeutic cargo release

Hitomi Hosoya[a,b,1], Andrey S. Dobroff[c,d,1], Wouter H. P. Driessen[e,1,2], Vittorio Cristini[f,g,h], Lina M. Brinker[c,d], Fernanda I. Staquicini[c,d], Marina Cardó-Vila[c,d], Sara D'Angelo[i,3], Fortunato Ferrara[i,3], Bettina Proneth[e,4], Yu-Shen Lin[j], Darren R. Dunphy[k,l], Prashant Dogra[c,d], Marites P. Melancon[h], R. Jason Stafford[h], Kohei Miyazono[a], Juri G. Gelovani[m], Kazunori Kataoka[a,n], C. Jeffrey Brinker[c,k,l,o], Richard L. Sidman[p,5], Wadih Arap[c,q,5,6], and Renata Pasqualini[c,d,5,6]

[a]Department of Molecular Pathology, Graduate School of Medicine, The University of Tokyo, Tokyo 113-8656, Japan; [b]The University of Tokyo Hospital, Tokyo 113-8656, Japan; [c]University of New Mexico Comprehensive Cancer Center, Albuquerque, NM 87131; [d]Division of Molecular Medicine, Department of Internal Medicine, University of New Mexico School of Medicine, Albuquerque, NM 87131; [e]David H. Koch Center, The University of Texas M.D. Anderson Cancer Center, Houston, TX 77030; [f]Department of NanoMedicine and BioMedical Engineering, School of Medicine, The Brown Foundation Institute of Molecular Medicine, The University of Texas Health Science Center at Houston, Houston, TX 77054; [g]Department of Proteomics and Systems Biology, The Brown Foundation Institute of Molecular Medicine, The University of Texas Health Science Center at Houston, Houston, TX 77054; [h]Department of Imaging Physics, The University of Texas M.D. Anderson Cancer Center, Houston, TX 77054; [i]Bioscience Division, Los Alamos National Laboratory, Los Alamos, NM 87545; [j]Oncothyreon, Seattle, WA 98121; [k]Center for Micro-Engineered Materials, University of New Mexico, Albuquerque, NM 87131; [l]Sandia National Laboratories, Albuquerque, NM 87106; [m]Department of Biomedical Engineering, Wayne State University, Detroit, MI 48201; [n]Department of Bioengineering, Graduate School of Engineering, The University of Tokyo, Tokyo 113-8656, Japan; [o]Department of Chemical and Nuclear Engineering, University of New Mexico, Albuquerque, NM 87131; [p]Harvard Medical School and Department of Neurology, Beth Israel Deaconess Medical Center, Boston, MA 02215; and [q]Division of Hematology/Oncology, Department of Internal Medicine, University of New Mexico School of Medicine, Albuquerque, NM 87131

Contributed by Richard L. Sidman, January 6, 2016 (sent for review December 7, 2015; reviewed by Steven A. Curley and José N. Onuchic)

A major challenge of targeted molecular imaging and drug delivery in cancer is establishing a functional combination of ligand-directed cargo with a triggered release system. Here we develop a hydrogel-based nanotechnology platform that integrates tumor targeting, photon-to-heat conversion, and triggered drug delivery within a single nanostructure to enable multimodal imaging and controlled release of therapeutic cargo. In proof-of-concept experiments, we show a broad range of ligand peptide-based applications with phage particles, heat-sensitive liposomes, or mesoporous silica nanoparticles that self-assemble into a hydrogel for tumor-targeted drug delivery. Because nanoparticles pack densely within the nanocarrier, their surface plasmon resonance shifts to near-infrared, thereby enabling a laser-mediated photothermal mechanism of cargo release. We demonstrate both noninvasive imaging and targeted drug delivery in preclinical mouse models of breast and prostate cancer. Finally, we applied mathematical modeling to predict and confirm tumor targeting and drug delivery. These results are meaningful steps toward the design and initial translation of an enabling nanotechnology platform with potential for broad clinical applications.

ligand receptor | mathematical modeling | nanoparticle | phage display | photothermal therapy

Significance

The main goal in the emerging field of cancer nanomedicine is to generate, standardize, and produce multifunctional carriers designed to improve the response of drugs against tumors. Here we report the design, development, and preclinical validation of a ligand-directed bioinorganic platform that integrates tumor targeting, receptor-mediated cell internalization, photon-to-heat conversion, and drug delivery. This enabling hydrogel-based technology can accommodate a broad variety of ligands, nanoparticles, and payloads. We show experimental proof-of-concept in mouse models of breast and prostate cancer with molecular imaging and marked reduction of tumor growth. However, with future proof that this technology is translatable, medical applications beyond cancer may also be leveraged.

A long-term goal in contemporary cancer nanomedicine has been to design and generate drug delivery systems that improve the narrow therapeutic window associated with conventional chemotherapeutics (1, 2). Conceptually, several nanotechnology-based entity candidates, including protocells (3), biosynthetic nanoparticles (NPs), viruses, and liposome-based nanoparticles, could be targeted for active delivery through a defined cell surface ligand receptor system and/or physically triggered for finely tuned cargo release (2, 4, 5).

Numerous efforts have been made to functionalize NPs by combining them with antibodies, aptamers, peptides, vitamins, or carbohydrates (6–8), but the majority of studies involve untargeted nanoplatforms (4, 9). In practice, targeting NPs is far from trivial, and ongoing challenges include synthesis and purification, selection of an appropriate ligand receptor, and specific composition for NP conjugation. Even the conjugation reaction itself may alter the binding of the tumor-targeting moiety to its receptor through conformational changes, steric freedom restriction, or orientation distortion (10, 11). Unfortunately, the

Author contributions: H.H., A.S.D., W.H.P.D., F.I.S., K.M., C.J.B., R.L.S., W.A., and R.P. designed research; H.H., A.S.D., W.H.P.D., L.M.B., F.I.S., M.C.-V., S.D., F.F., B.P., Y.-S.L., D.R.D., P.D., M.P.M., and R.J.S. performed research; V.C., K.M., J.G.G., K.K., C.J.B., and R.L.S. contributed new reagents/analytic tools; H.H., A.S.D., W.H.P.D., V.C., M.P.M., J.G.G., K.K., C.J.B., R.L.S., W.A., and R.P. analyzed data; H.H., A.S.D., W.H.P.D., V.C., F.I.S., C.J.B., R.L.S., W.A., and R.P. wrote the paper; and V.C. and P.D. developed the mathematical model.

Reviewers: S.A.C., Baylor College of Medicine; and J.N.O., Rice University.

Conflict of interest statement: C.J.B. declares that the protocell nanocarrier technology is exclusively licensed by Oncothyreon Inc. (Seattle, WA). W.A. and R.P. are inventors on patents filed on the technology and intellectual property reported here, which have been licensed to Arrowhead Research Corporation. W.A. and R.P. are entitled to standard royalties if commercialization occurs. The University of New Mexico currently manages these arrangements in accordance with its established institutional conflict of interest policy.

Freely available online through the PNAS open access option.

[1]H.H., A.S.D., and W.H.P.D. contributed equally to this work.

[2]Present address: Roche Pharma Research and Early Development, Roche Innovation Center Basel, 4070 Basel, Switzerland.

[3]Present address: University of New Mexico Comprehensive Cancer Center, Division of Molecular Medicine Department of Internal Medicine, University of New Mexico School of Medicine, Albuquerque, NM 87131.

[4]Present address: Helmholtz Zentrum München, Institute of Developmental Genetics, 85764 Neuherberg, Germany.

[5]To whom correspondence may be addressed. Email: richard_sidman@hms.harvard.edu, warap@salud.unm.edu, or rpasqual@salud.unm.edu.

[6]W.A. and R.P. contributed equally to this work.

This article contains supporting information online at www.pnas.org/lookup/suppl/doi:10.1073/pnas.1525796113/-/DCSupplemental.

cost-to-benefit ratio of these modifications often elevate the complexity of the NP synthesis, complicating regulatory hurdles because of formulations that are heterogeneous or difficult to reproduce (10, 12, 13).

To minimize such drawbacks, NPs can be functionalized via virus-based nanoplatforms as an alternative for targeted cargo delivery (14–16). In particular, filamentous bacteriophage (phage)—a prokaryotic virus—is an attractive candidate to develop a bionanomedicine for cancer therapeutics because phage particles are cost-effectively produced with biological uniformity, as well as being physically robust and stable under harsh conditions (17). Notably, phage-based nanoplatforms are biocompatible and nonpathogenic with eukaryotic organisms and are able to preserve the desired cell targeting and internalization (18). Moreover, phage particles are ideal for incorporating other NPs, which can be released after reaching the tumor site. An admixture of colloidal gold NP (AuNP) with phage particles spontaneously organizes into hydrogel network-like fractal structures (19, 20). These hydrogel networks offer convenient multifunctional integration within a single entity for tumor targeting, enhanced fluorescence and dark-field microscopy, near-infrared (NIR) photon-to-heat conversion, and surface-enhanced Raman scattering (SERS)-based detection (20, 21).

In the present work, we developed a tumor targeting theranostic (meaning a combination of therapeutics and diagnostics) hydrogel-based nanoplatform that enables ligand-directed tumor targeting, multimodal imaging capability, and triggered therapeutic cargo release. Our data suggest that targeted hydrogel photothermal therapy represents a functional theranostic approach (fostering "see and treat, treat and see") in the diagnosis and management of tumors.

Results

Essential Functional Attributes of the Nanoplatform (I): Temperature-Sensitive Cargo Release. We set out to design and generate a targeted hydrogel photothermal nanotherapy platform that would release therapeutic cargo to tumors after NIR laser-triggered heating by incorporating heat sensitive-based liposome (HSL) (22) formulations into targeted phage-based hydrogel networks (Fig. S1).

In proof-of-concept experiments, we evaluated several candidate systems at the nanoscale level—such as liposomal-based NPs, AuNP, mesoporous silica nanoparticles (MSNPs) (23), and phage-based systems—because they may be targeted by a ligand to a defined cell membrane receptor. HSLs were initially chosen because delivery of their contents can be triggered through temperature-sensitive mechanisms and, by formulating them with lipids with established phase-transition temperature (*SI Materials and Methods*), cargo release may be more finely tunable. Therefore, we selected a well-defined heat-sensitive formulation to achieve triggered release specifically at temperatures >40 °C. As a negative control, corresponding non-HSLs (*SI Materials and Methods*) were also formulated side-by-side and normalized by vesicle extrusion through a standard 100-nm-sized track-etched membrane.

To profile cargo release from the experimental (heat-sensitive) or control (non–heat-sensitive) liposomes, we loaded them with calcein (at a self-quenching concentration) to monitor the time- and temperature-dependent fluorescence release. Experimental and control liposomes were gradually heated from room temperature to 50 °C. As predicted, the heat-sensitive formulation released fluorescent calcein at temperatures above 40 °C, whereas the negative control remained intact up to 45 °C (Fig. 1*A*). Next, the temperature was kept constant at 42 °C, and calcein release was monitored over time. Fluorescent calcein was released within 10 min from HSLs; in contrast, negative control non–HSLs retained >90% of their contents for the 30-min experimental duration (Fig. 1*B*), showing temperature-sensitive test cargo release from HSL.

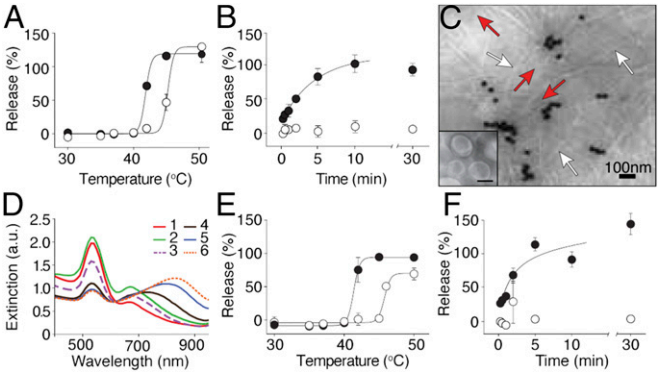

Fig. 1. Generation and functional characterization of HSL-containing hydrogels. (*A* and *B*) The release profile of HSL (●) and non-HSL (○) on heating was assessed by the quenching properties of calcein. Percent release as a function of temperature (*A*) and the time course of release at 42 °C (*B*) were measured (80% within 5 min; 100% within 10 min). (*C*) HSL-containing hydrogels were observed by TEM (red arrows: HSL; white arrows: phage particles; dark particles: AuNP). (*Inset*) HSL alone. (Scale bar, 50 nm.) (*D*) UV-vis spectra at serial phage titers (1–6), starting from 7.5×10^7 TU/μL and diluted 1:4 sequentially to 7.3×10^4 TU/μL. (*E* and *F*) Release profiles of HSL- (●) and non–HSL- (○) containing hydrogels as a function of temperature (*E*) and temporal release profile at 42 °C (*F*). Shown data are mean ± SEM.

Essential Functional Attributes of the Nanoplatform (II): Hydrogel Assembly. Having demonstrated the differential time- and temperature-dependent release of cargo from HSL relative to the corresponding negative control non-HSLs, we subsequently generated a nanocarrier-based version through the optimal integration of self-assembled hydrogels (19, 20) (Fig. S2) consisting of AuNP and phage particles plus HSLs (named henceforth HSL-containing hydrogels).

Transmission electron microscopy (TEM) analysis (Fig. 1*C*), as well as optical and NIR surface-enhanced Raman scattering (NIR-SERS) profiling, confirmed the physical elements of the HSL-containing hydrogel (Fig. 1*D* and Fig. S3). As the hydrogel is formed (dilutions 5 and 6; Fig. 1*D*), a gradual reduction in absorption occurs at 520 nm accompanied by an increase in absorption in the NIR region (800–900 nm). This absorbance is plausibly attributed to the coupled plasmon resonance of the hydrogel as the interparticle distance (d_{Au}) becomes gradually smaller than the particle radius during self-assembly and clustering (24). We subsequently assessed whether the integrity- and temperature-dependent release of HSLs was maintained when incorporated into hydrogels. Both the overall cargo release profile and the release kinetics of calcein were essentially indistinguishable from those observed for HSLs alone (Fig. 1 *E* and *F*).

Essential Functional Attributes of the Nanoplatform (III): NIR-Triggered Cargo Release. Given that hydrogels have photon-to-heat converting properties and possess a broad absorption band in the NIR region (20), we next investigated whether the HSL-containing hydrogels would also exhibit temperature-stimulated release on NIR irradiation in an in vitro agarose gel phantom model (*SI Materials and Methods*).

On NIR laser illumination (808-nm fiber-coupled diode NIR), a positive temperature differential was observed for hydrogel embedded in phantoms relative to either HSLs or AuNP alone (Fig. 2*A*). Moreover, termination of NIR laser stimulation caused a gradual temperature drop back to baseline, illustrating that the temperature differential was dependent on the interaction between the NIR laser and hydrogel. These data demonstrate that hydrogels have elastic properties that allow reversible laser-based heating without loss of physical integrity under the experimental conditions used. To assess the effect of

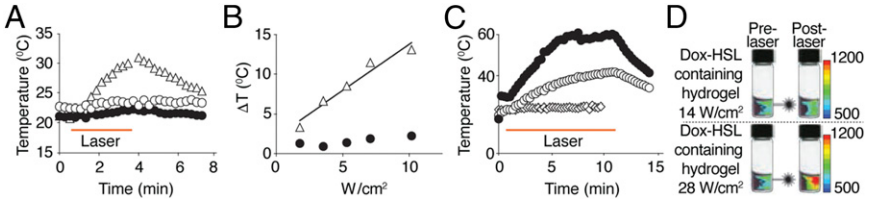

Fig. 2. NIR laser illumination of hydrogel assembly. (*A*) Hydrogel (△) was solidified in agarose gel phantoms and tested for heat formation on NIR laser illumination at 5.3 W/cm^2 for 3 min. HSL (○) or AuNP (●) was used as a control. Temperature was monitored with a thermocouple probe. (*B*) The correlation of NIR laser irradiation and temperature elevations between hydrogel (△) and AuNP (●) was examined. (*C*) HSL-containing hydrogels in phantoms were examined for heat formation with NIR laser illumination at 28 (●) and 14 W/cm^2 (○) for 10 min. HSL (◇) illuminated with NIR laser at 14 W/cm^2 was used as a control. (*D*) To visualize dox release from hydrogels, fluorescence intensity of λex/λem = 470/600 nm was measured before (prelaser) and after NIR laser (postlaser) illumination for 10 min at 14 or 28 W/cm^2. Relative fluorescent units (RFUs) are indicated by color bars.

photon dose on the temperature differential in the phantom assays, hydrogels underwent exposure to increasing NIR laser power density and/or time interval (Fig. 2*B*). We identified a positive correlation between temperature differential and photon dose (Fig. 2*B*), which was absent in AuNP (negative control).

To evaluate whether HSL-containing hydrogels would also maintain photon-to-heat conversion properties, either HSL-containing hydrogels or HSL alone (control) embedded phantom vials were submitted to 14- or 28-W/cm^2 laser-driven NIR power densities over 10 min. At a NIR laser power density of 14 W/cm^2, the temperature of the hydrogel increased twofold (Fig. 2*C*). Further, when heated at 28 W/cm^2, the temperature of the HSL-containing hydrogel increased threefold compared with HSL alone.

We next evaluated whether the heat produced by the hydrogel-NIR laser interaction could trigger the release of encapsulated material. To this end, hydrogels were formed with the cytotoxic chemotherapeutic drug doxorubicin (dox), encapsulated with HSL, and embedded in phantoms. We used a multispectral fluorescent imaging system to visualize the induced release of dox. On illumination with NIR (14- and 28-W/cm^2 power densities), a reproducible and robust photon dose-dependent increase in fluorescence intensity was observed. These data demonstrate NIR laser-triggered drug release of HSL-containing hydrogels (Fig. 2*D*).

Magnetic Resonance Temperature Imaging of Temperature Elevation and Triggered Heat-Sensitive Liposome Release. To assess the NIR laser-induced spatiotemporal heat distribution, magnetic resonance temperature imaging (MRTI) was performed (Fig. 3*A*). HSL-containing hydrogels were embedded in agarose gel phantoms with a NIR laser positioned perpendicular to the sample. Spatiotemporal heat distribution and heat expansion of HSL-containing hydrogels were documented and analyzed by MRTI on laser treatment (Fig. 3*B*). Quantification of a region of interest (ROI) further revealed that the temperature rapidly increased by 38 °C within 150 s (Fig. 3*B, Lower*). Additionally, because a consistent drop in temperature was observed when NIR laser illumination was terminated, these results indicate that the heat production occurs exclusively during NIR laser activation.

To evaluate visually the content release from HSL-containing hydrogels in vitro, gadolinium (Gd-DTPA)-encapsulated-HSLs served as a surrogate marker for T1-weighted imaging (T1WI). T1 mapping was performed before and after laser illumination (Fig. 3*C*). A decrease in T1 relaxation time was observed in the heated region (>42 °C, calculated based on MRTI), where the average T1 relaxation time in the ROIs was 400.6.±10.8 ms before and 312.3 ± 6.1 ms after NIR laser treatment (Fig. 3*C, Lower*), confirming the release of Gd-DTPA in the region where the temperature increased to >42 °C.

Targeting Hydrogels in Vitro. We showed that spatial and temporal control of cargo release from hydrogels can be achieved by NIR illumination. However, without active ligand-directed capabilities, one would be limited to local/regional administration of HSL-containing hydrogels or, perhaps in some cases, would be dependent on the enhanced permeability and retention (EPR) effect (25, 26). Therefore, to provide active targeting features to HSL-containing hydrogel systems, a ligand consisting of a well-established cyclic peptide (sequence YRCTLNSPFFWEDM-THECHA), which binds to the chicken tumor virus no.10 regulator of kinase-like protein (CRKL), was inserted into the phage-displayed portion of the hydrogel (27). CRKL-binding phage particles specifically and strongly target EF43.*fgf-4* mammary carcinoma cells (27). Thus, we first verified that the particle targeting capability was indeed preserved by incubating either targeted or nontargeted hydrogels with EF43.*fgf-4* cells (Fig. 4*A* and Fig. S4*A*).

Next, we examined whether the targeted particles maintained their inherent peptide-mediated binding properties in HSL-containing hydrogels by using rhodamine-labeled test HSLs. Side-by-side immunostaining experiments showed efficient cell internalization of targeted phage particles but not untargeted control particles (Fig. 4*B* and Fig. S4*B*), confirming that ligand targeted phage particles do not lose functional capabilities in the context of HSL-containing hydrogels. To analyze the subcellular localization of targeted HSL-containing hydrogel after internalization, we performed TEM with EF43.*fgf-4* tumor cells. AuNP clusters were observed within the endosomal compartments (Fig. 4*C*, red arrows), further substantiating the immunostaining showing internalization of targeted HSL-containing hydrogels.

Tracking Hydrogels in Vivo. To evaluate the whole-body biodistribution of targeted HSL-containing hydrogel noninvasively, we next incorporated NIR-labeled heat-sensitive liposomes into

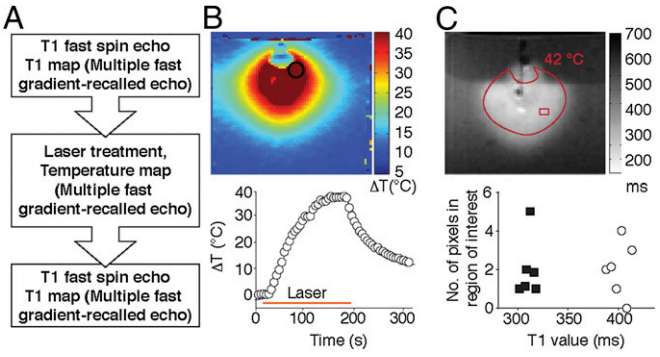

Fig. 3. Triggered agent release by NIR. (*A*) Experimental design of MRI and MRTI. (*B*) Temperature change of hydrogel-containing gel (phantom) measured by MRTI on NIR laser treatment is shown in color scale. The time course of ROI (indicated by a circle) is shown below. (*C*) T1-weighted image shows a region with high signal intensity, which suggests that Gd-DTPA-HSL released the contents on laser treatment. This area overlapped the region that reached >42 °C. Prelaser T1 value (○); Postlaser T1 value (■).

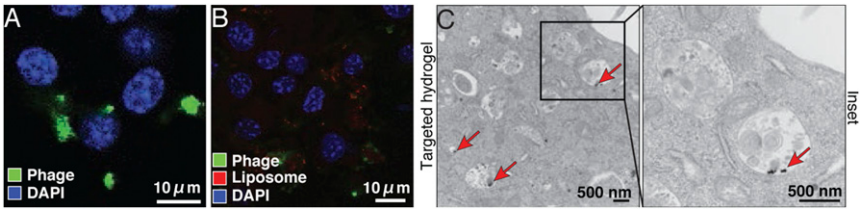

Fig. 4. Tumor cell internalization of targeted HSL-containing hydrogels. (*A*) EF43.*fgf-4* cells were incubated with CRKL-targeted or nontargeted hydrogels for 24 h and stained with antiphage antibodies and with DAPI for nuclei. Internalized phage particles were observed by confocal microscopy. (*B*) EF43.*fgf-4* cells were incubated with CRKL-targeted HSL-containing hydrogels to examine targeting capabilities. Liposomes were visualized by rhodamine fluorescence in the bilayers of the liposomes. (*C*) TEM images of EF43.*fgf-4* cells treated with CRKL-targeted HSL-containing hydrogels. Red arrows indicate internalized AuNP.

the targeted hydrogel formulation and administered it systemically (i.v.) into BALB/c mice bearing EF43.*fgf-4* mammary carcinoma. Optical imaging was performed at 1, 7, and 24 h after administration. Tumor-bearing mice that received targeted HSL-containing hydrogels had an average tumor fluorescent intensity 160% higher than those that received nontargeted HSL-containing control hydrogels (Fig. 5 *A* and *B*). To validate these results histologically, rhodamine-labeled HSLs were used with either targeted or nontargeted HSLs and again were administered into tumor-bearing mice. Tumors were collected after 24 h, and sections were stained with antiphage and CD34 antibodies and observed by confocal and dark-field microscopy. Robust intracellular accumulation of AuNP, targeted phage, and HSLs were observed within the tumor sections compared with negative controls (Fig. 5*C*).

Triggered Heat Generation and NIR-Induced Cargo Release in Vivo. We next sought to evaluate whether accumulated hydrogels in tumors could exhibit temperature-stimulated release on NIR laser illumination. Targeted hydrogel, AuNP, or PBS vehicle was administered i.v. to EF43.*fgf-4* tumor-bearing mice. After 24 h, NIR laser (3.5 W/cm^2) treatment was applied for 3 min, and intratumoral temperature was serially monitored with a thermocouple probe. As depicted in Fig. 6*A*, an intratumoral temperature increase of 4.6 °C was observed during NIR laser application in tumor-bearing mice treated with targeted hydrogel relative to those receiving AuNP (14.2 ± 6.3 °C vs. 9.6 ± 2.8 °C; $^*P < 0.05$). No laser damage of the skin was noted either macroscopically or microscopically.

Next, we administered targeted dox-HSL–containing hydrogels or dox-HSL alone to EF43.*fgf-4* tumor-bearing mice and treated the tumors with NIR laser for 3 min at 3.5 W/cm^2 (Fig. 6*B*). Mice receiving targeted dox-HSL–containing hydrogel showed rapid elevations in intratumoral temperature, reaching 45 °C within 3 min of NIR laser treatment, whereas mice treated with dox-HSL (negative control) showed no detectable intratumoral temperature increase.

To assess heat distribution and tumor treatment efficacy of the targeted hydrogels, we designed and prepared a targeted hydrogel formulation (sensor/reporter) by using Gd-DTPA–encapsulated (0.5 mmol/mL) and NIR dye-labeled HSLs as a surrogate marker of drug release and a tracking agent for real-time optical imaging (Fig. S5*A*). Targeted particle accumulation in tumors was observed after 24 h of hydrogel administration. Tumors were subsequently exposed to NIR laser application at 3.5 W/cm^2 for 3 min, and tumor temperature was monitored by MRTI. In line with the previous thermocouple measurement results, temperature elevations of 7–13 °C within the tumor tissue were noted (Fig. 6*C*). These data are consistent with gold nanoshell reports that heat generation on NIR laser illumination occurs in a localized area with only minimal or no heat conduction to surrounding tissues (28). To visualize the release of Gd-DTPA from HSL, T1 mapping was performed before and after NIR laser illumination. Decreases in T1 relaxation time were observed in the tumor ROI (Fig. S5*B*), with times averaging 518.9 ± 43.0 ms before and 457.6 ± 48.1 ms after NIR laser treatment (Fig. 6*D*).

Antitumor Activity of Targeted Hydrogel Formulations. The antitumor effect of targeted hydrogel delivery with subsequent NIR laser irradiation (photothermal therapy) was evaluated in comparison with conventional dox-HSL treatment (Fig. 6*E*). A single dose of targeted dox-HSL–containing hydrogel, dox-HSL only, or vehicle (PBS) alone was administered systemically (i.v.) into EF43.*fgf-4* tumor-bearing mouse cohorts (day 11, black arrow). Photothermal therapy at 3.5 W/cm^2 for 3 min (day 12, red arrow) began 24 h after administration. Tumor growth was reduced in tumor-bearing mouse cohorts receiving the targeted dox-HSL–containing hydrogel compared with control mice receiving dox-HSL (mean tumor volumes at day 12; 88.0 vs. 140.4 mm^3, respectively). Moreover, inhibition of tumor growth persisted to day 21 in mice injected with the targeted dox-HSL–containing hydrogel compared with either dox-HSL or vehicle (mean tumor volumes at day 21; 185.4, 599.9, and 764.4 mm^3, respectively; $^{**}P < 0.01$ and $^{***}P < 0.001$).

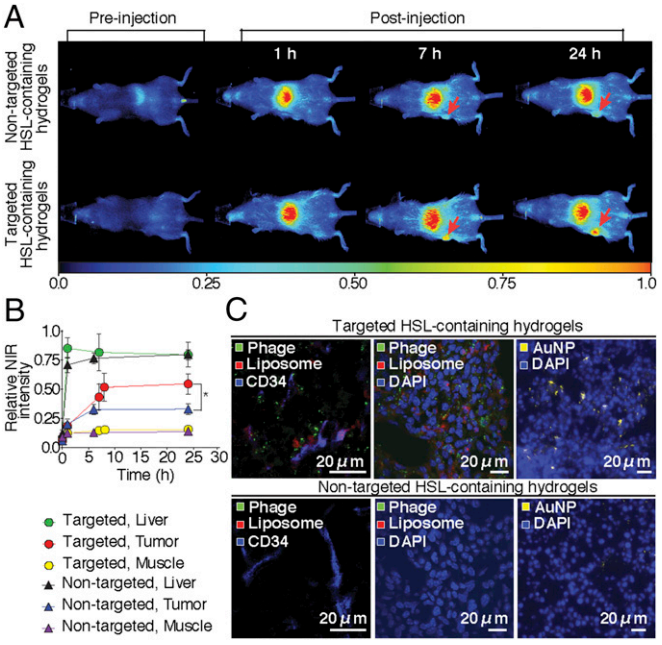

Fig. 5. Hydrogel homing to tumors in vivo. (*A*) Targeted or nontargeted hydrogels were injected into EF43.*fgf-4* tumor-bearing mice and tracked by optical imaging from the ventral side. (*B*) The accumulation of hydrogels was quantified as a mean intensity of NIR signal in tumor, liver, and muscle. Shown data are mean ± SEM; $^*P < 0.01$. (*C*) Tumor tissue sections after 24 h of hydrogel administration are shown. Phage particles were detected with antiphage antibody (green), liposomes (red), AuNP (dark field microscopy, yellow), vascular endothelial cells (anti-CD34 antibody, blue), and cell nuclei with DAPI (blue).

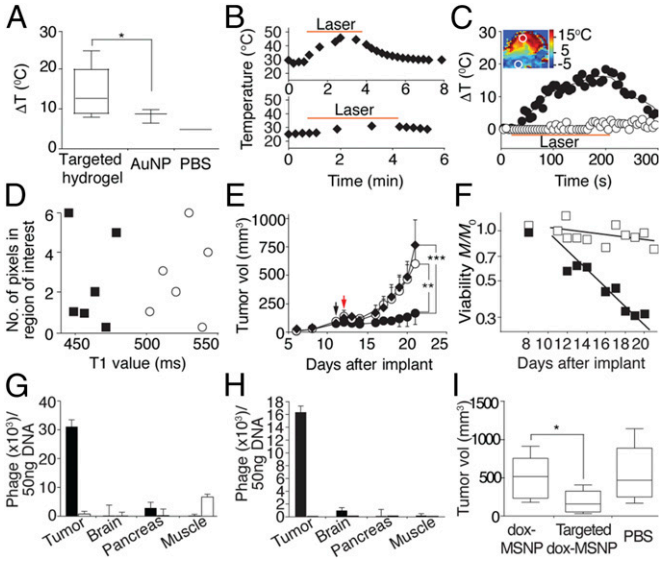

Fig. 6. Targeted photothermal therapy in preclinical models of breast and prostate cancer. (*A*) Targeted hydrogels were injected in vivo and the NIR laser was illuminated after 24 h with the power density set at 3.5 W/cm^2 (*$P < 0.05$). Box-and-whiskers plots, median line; box, quartiles; whiskers, 5–95% confidence. (*B*) Targeted dox-HSL–containing hydrogels (*Upper*) or dox-HSL alone (*Lower*) were administered to mouse cohorts, and the temperature changes during NIR laser illumination at 3.5W/cm^2 were monitored. (*C*) The NIR laser illuminated tumors while MRTI was performed. The largest temperature change during NIR laser illumination was mapped (*Inset*). The time course of temperature changes in the ROI in tumor and nonmalignant tissue. Tumor region (●); nontumor region (○). (*D*) T1 mapping of a tumor section before (○) and after (■) the NIR laser treatment. (*E*) The tumor treatment effect of targeted dox-HSL–containing hydrogel (●) photothermal therapy was evaluated relative to dox-HSL (○) or PBS (♦) treatment. Black arrow, hydrogel administration; red arrow; NIR laser treatment at 3.5 W/cm^2 for 3 min (shown data are mean ± SEM; **$P < 0.01$, ***$P < 0.001$; $n = 7$). (*F*) Logplot of viability data M/M_0 for targeted hydrogel delivery (■) as a fraction of PBS controls vs. time ($P = 0.00019$, $R^2 = 0.98$). For comparison, the dox-HSL (□) results are also shown ($P = 0.0018$, $R^2 = 0.98$). (*G* and *H*) Delivery of targeted (■) and control (□) FITC-MSNP–containing hydrogel to EF43.*fgf-4* tumor-bearing mice (*G*) and DU145 tumor-bearing mice (*H*) (shown data are mean ± SEM; $n = 8$). (*I*) Targeted dox-MSNP–containing hydrogels in EF43.*fgf-4* tumor-bearing mice gives a tumor growth delay (*$P < 0.05$; $n = 8$).

Predictive Correlation of Tumor Response: Mathematical Modeling and Validation. To substantiate our findings in vivo, we used a mechanistic mathematical model (*SI Materials and Methods*) of drug transport through the tumor interstitium and fitted it to predict and verify the corresponding tumor response. The underlying biophysical processes can be arithmetically defined by the exponential death rate equation (e^x death rate $= \lambda_K \cdot \sigma_U$) to determine the potential efficacy of a given chemotherapy drug, where λ_K is the biological property of the pair cell type/drug type, and σ_U is the physical property of the tumor parenchyma, stroma, and its associated microenvironment, in which processes such as convection, diffusion (29–31), and cell membrane crossing (32) determine how much drug is available for uptake by the tumor.

The central hypothesis of the model is that the death rate of a cell population is proportional to total amount of drug uptake over time—i.e., the time integral of the rate of drug uptake by the tumor cells—where cells reach a constant rate of death, which is exponential in time (30). Thus, the decrease of total tumor mass (M) as a function of time can be expressed as $M \sim e^{-\lambda_K \cdot \sigma_U \cdot t}$. By fitting this equation to the data for targeted dox-HSL–containing hydrogels (Fig. 6*F*, solid square) or dox-HSL (Fig. 6*F*, empty square) against vehicle (negative control), one obtains the "kill" time $(\lambda_K \cdot \sigma_U)^{-1} \cong 8$ d or $(\lambda_K \cdot \sigma_U)^{-1} \cong 55$ d, respectively. These results show that hydrogels markedly increased the rate of tumor death by ∼700% compared with conventional HSL delivery. Moreover, considering the tumor volume $V_0 \cong 85$ mm^3 and the calculated mass of dox delivered in vivo equals to $F \cdot t_K = 0.037$ mg (where F is the total rate of release from the nanoparticles and t_K is the total exposure time of the cells to the drug), the total uptake within the tumor was calculated as $\sigma_U \equiv F \cdot t_K / V_0 \cong 750$ μM with the time integral over time of exposure being $\sigma_U \cdot t_K \cong 17.7$ mM/d. By analyzing the in vitro data by using $IC_{100} \cong 2$ μM of dox, the correspondent in vivo tumor concentration of used drug was $\sigma_U \cong 25$ mM within a time of exposure equals to $t_K \cong 1$ d (note that the equivalent tumor concentration is different from the drug concentration IC in vitro, the relationship being the total volume of solution in vitro was 100 μL and the 8×10^3 cells exposed to drug roughly occupy a volume of ∼0.008 μL). Therefore, the equivalent time integral over time of exposure shown in vitro was approximately 25 mM/d, of the same order of magnitude as the corresponding value found in vivo (17.7 mM).

Given that the tumor growth was markedly reduced after treatment, the mathematical model introduced here clearly indicates that the superior features of the targeted dox-HSL–containing hydrogel is due to its ability to deliver a greater amount of dox-loaded HSL to tumors than the appropriate controls. By accounting for the critical physical transport issues, one could speculate that our mathematical model is able to predict the behavior of targeted delivery systems based on hydrogel nanoplatforms.

Design and Translational Development of Alternative Targeted Hydrogel Formulations Based on Mesoporous Silica Nanoparticles. To further increase the versatility of the hydrogel-based nanoplatform introduced here, we also designed, generated, and evaluated alternative nanoscale materials, namely a hydrogel prepared by electrostatically mediated self-assembly of phage particles, AuNP, and MSNP (33, 34). Fig. S5*C* shows a cryo-TEM image of the MSNP-containing hydrogel, and the *Inset* indicates the ordered arrangement of 2.5-nm-diameter cylindrical pores that comprise the MSNP framework.

A major advantage of MSNPs, which are negatively charged at neutral pH ($pK_a = 3$, ζ-potential = −35.2 mV) due to deprotonation of surface silanols (≡Si-OH), is that their internal porosity provides an enormous surface area (>1,000 m^2/g) on which to adsorb disparate types of cargo combinations through van der Waals, electrostatic, or hydrogen-bonding interactions (23). Previous reports have shown that owing to the high pK_a of dox (8.25), it electrostatically associates with the negatively charged MSNP, resulting in orders of magnitude greater loading than in standard liposomes (35). For electrostatically associated cargos (and strongly adsorbed cargos in general), the drug release is mediated in part by the dissolution of the amorphous silica framework—to form nontoxic silicic acid $Si(OH)_4$—thus enabling sustained release. The use of MSNPs is central for optimizing treatment according to recent experimental models showing that the integrated drug uptake profile by the cells over time is indeed a key determinant of the dose–response relationship.

Antitumor Activity of Mesoporous Silica Nanoparticles-Based Formulation in Preclinical Models of Breast and Prostate Cancer. As proof-of-concept, we similarly evaluated the homing properties of these alternative hydrogel formulations for in vivo payload delivery of FITC in two cancer models: the EF43.*fgf-4* syngeneic model of breast cancer and the DU145-derived xenograft model of prostate cancer. A strong glucose-regulated protein-78 (GRP78)-binding motif (sequence CSNTRVAPC) served as an established ligand moiety for in vivo targeted delivery to vascular endothelial cells and tumor cells (36). Targeted FITC-MSNP-containing hydrogels bound 6-fold more to EF43.*fgf-4* isogenic mammary carcinoma (immunocompetent mouse host; Fig. 6*G*), and 16-fold more to DU145-derived tumor xenograft (immunodeficient mouse host; Fig. 6*H*) compared with the control untargeted hydrogels. Moreover, binding to control brain, pancreas,

and muscle was borderline detectable (Fig. 6*G*). Fig. S5*D* illustrates representative images of FITC-loaded MSNPs in human DU145-derived tumor xenografts.

Next, we evaluated the translational potential of this platform by testing the delivery of loaded MSNP (dox-MSNP) in a targeted hydrogel to tumor models (Fig. 6*I*). Control groups included treatment with dox-MSNP alone, and vehicle (PBS) alone. A robust and significant reduction in tumor growth was observed in animals treated with targeted dox-MSNP–containing hydrogels relative to negative control groups.

Discussion

We introduce a targeted theranostic nanoplatform that integrates peptide-targeted phage particles, photon-to-heat conversion, and HSL or MSNP into a ligand-directed hydrogel that carries and delivers both diagnostic agents and therapeutic drugs. The early translational results presented here indicate that either HSL or MSNP maintain their essential physical attributes, contents, and heat-sensitive releasing function on NIR laser treatment after incorporation into targeted hydrogels. We demonstrate that HSL-containing hydrogels generate heat only locally on NIR laser illumination in vivo so that the spatially restricted rise in temperature leads to localized release of hydrogel contents on photothermal command in a remarkably superior manner relative to negative controls. The versatility of this enabling nanotechnology allows design of different formulations of assorted ligands (such as binding peptide motifs, peptidomimetic-inspired drugs, and monoclonal antibodies) at rates designated in advance for tumors of various sizes, growth rates, and cell types. MSNPs were successfully incorporated into targeted hydrogels, and with systemic administration, clearly reduced xenografted human tumors with no evident off-target effects, encouraging speculation that the further incorporation of heat-sensitive lipid compositions within ligand peptide-targeted MSNP-containing hydrogels, will allow one to attain greater control by suppressing drug leakage without NIR irradiation and greater cytotoxic activity due to a superior drug capacity released with NIR irradiation. The hydrogel-based nanoplatforms described here and mathematically validated have potential for translation into theranostic clinical applications such as image-guided approaches to diagnostic and therapeutic monitoring (see and treat, treat and see), and ultimately the targeted delivery of several therapeutic nanomaterials against malignant tumors and other human diseases.

Materials and Methods

Animals. BALB/c and BALB/c nude mice (6–8 wk) were purchased from Charles River. All animal work followed standard procedures approved by The University of Texas M.D. Anderson Cancer Center and the University of New Mexico Institutional Animal Care and Use Committee.

Cryo-TEM. The cryo-TEM sample was prepared with an FEI Vitrobot Mark IV on a Quantifoil R1.2/1.3 holey carbon grid, using a sample volume of 4 μL, a blot force of 1, and blot and drain times of 4 and 0.5 s, respectively. Imaging was acquired with a JOEL 2010 TEM at 200 kV equipped with a Gatan model 626 cryo stage.

Statistical Analysis. Statistics were analyzed with GraphPad Prism (GraphPad). A Student *t* test served to evaluate the in vitro data statistically. Statistical analysis of the animal study results was performed with a two-way ANOVA. $P < 0.05$ was considered statistically significant.

Additional methods are described in *SI Materials and Methods*.

ACKNOWLEDGMENTS. We thank Dr. Andrew R. M. Bradbury (Los Alamos National Laboratories) for critical reading of this manuscript. This study was supported by the Japan Society for the Promotion of Science fellowships (to H.H.), National Science Foundation Grant DMS-1562068 (to V.C.), National Institutes of Health (NIH) Grants 1U54CA149196 and 1U54CA143907 (to V.C.), Lymphoma Leukemia Society Grant 7010-14 SCOR (to C.J.B.), NIH U01 CA151792-01 (C.J.B.), Oncothyreon (C.J.B.), NIH Grants R01U54CA143837 (to V.C., W.A., and R.P.), 1U54CA151668 (to V.C., W.A., and R.P.), and P50 CA140388 (to W.A. and R.P.), and awards from the Gillson–Longenbaugh Foundation and the Prostate Cancer Foundation (to W.A. and R.P.).

1. Nichols JW, Bae YH (2012) Odyssey of a cancer nanoparticle: From injection site to site of action. *Nano Today* 7(6):606–618.
2. Kumari P, Ghosh B, Biswas S (2016) Nanocarriers for cancer-targeted drug delivery. *J Drug Target* 24(3):179–191.
3. Liu J, Stace-Naughton A, Jiang X, Brinker CJ (2009) Porous nanoparticle supported lipid bilayers (protocells) as delivery vehicles. *J Am Chem Soc* 131(4):1354–1355.
4. Aslan B, Ozpolat B, Sood AK, Lopez-Berestein G (2013) Nanotechnology in cancer therapy. *J Drug Target* 21(10):904–913.
5. Prabhu RH, Patravale VB, Joshi MD (2015) Polymeric nanoparticles for targeted treatment in oncology: Current insights. *Int J Nanomedicine* 10:1001–1018.
6. Capolla S, et al. (2015) Targeted tumor imaging of anti-CD20-polymeric nanoparticles developed for the diagnosis of B-cell malignancies. *Int J Nanomedicine* 10:4099–4109.
7. Nicol JR, Dixon D, Coulter JA (2015) Gold nanoparticle surface functionalization: A necessary requirement in the development of novel nanotherapeutics. *Nanomedicine (Lond)* 10(8):1315–1326.
8. Kang B, et al. (2015) Carbohydrate-Based Nanocarriers Exhibiting Specific Cell Targeting with Minimum Influence from the Protein Corona. *Angew Chem Int Ed Engl* 54(25):7436–7440.
9. Müller LK, Landfester K (2015) Natural liposomes and synthetic polymeric structures for biomedical applications. *Biochem Biophys Res Commun* 468(3):411–418.
10. Cheng Z, Al Zaki A, Hui JZ, Muzykantov VR, Tsourkas A (2012) Multifunctional nanoparticles: Cost versus benefit of adding targeting and imaging capabilities. *Science* 338(6109):903–910.
11. Elias DR, Poloukhtine A, Popik V, Tsourkas A (2013) Effect of ligand density, receptor density, and nanoparticle size on cell targeting. *Nanomedicine (Lond)* 9(2):194–201.
12. Allen TM (2002) Ligand-targeted therapeutics in anticancer therapy. *Nat Rev Cancer* 2(10):750–763.
13. Shokeen M, et al. (2011) Evaluation of multivalent, functional polymeric nanoparticles for imaging applications. *ACS Nano* 5(2):738–747.
14. Galaway FA, Stockley PG (2013) MS2 viruslike particles: A robust, semisynthetic targeted drug delivery platform. *Mol Pharm* 10(1):59–68.
15. Koppers-Lalic D, Hogenboom MM, Middeldorp JM, Pegtel DM (2013) Virus-modified exosomes for targeted RNA delivery: A new approach in nanomedicine. *Adv Drug Deliv Rev* 65(3):348–356.
16. Smith MT, Hawes AK, Bundy BC (2013) Reengineering viruses and virus-like particles through chemical functionalization strategies. *Curr Opin Biotechnol* 24(4):620–626.
17. Christianson DR, Ozawa MG, Pasqualini R, Arap W (2007) Techniques to decipher molecular diversity by phage display. *Methods Mol Biol* 357:385–406.
18. Driessen WH, et al. (2010) On the synergistic effects of ligand-mediated and phage-intrinsic properties during in vivo selection. *Adv Genet* 69:115–133.
19. Souza GR, et al. (2008) Bottom-up assembly of hydrogels from bacteriophage and Au nanoparticles: The effect of cis- and trans-acting factors. *PLoS One* 3(5):e2242.
20. Souza GR, et al. (2006) Networks of gold nanoparticles and bacteriophage as biological sensors and cell-targeting agents. *Proc Natl Acad Sci USA* 103(5):1215–1220.
21. Souza GR, et al. (2006) In vivo detection of gold-imidazole self-assembly complexes: NIR-SERS signal reporters. *Anal Chem* 78(17):6232–6237.
22. Kim MS, et al. (2014) Temperature-triggered tumor-specific delivery of anticancer agents by cRGD-conjugated thermosensitive liposomes. *Colloids Surf B Biointerfaces* 116:17–25.
23. Tarn D, et al. (2013) Mesoporous silica nanoparticle nanocarriers: Biofunctionality and biocompatibility. *Acc Chem Res* 46(3):792–801.
24. Weisbecker CS, Merritt MV, Whitesides GM (1996) Molecular self-assembly of aliphatic thiols on gold colloids. *Langmuir* 12(16):3763–3772.
25. Maeda H (2015) Toward a full understanding of the EPR effect in primary and metastatic tumors as well as issues related to its heterogeneity. *Adv Drug Deliv Rev* 91:3–6.
26. Matsumura Y, Maeda H (1986) A new concept for macromolecular therapeutics in cancer chemotherapy: Mechanism of tumoritropic accumulation of proteins and the antitumor agent smancs. *Cancer Res* 46(12 Pt 1):6387–6392.
27. Mintz PJ, et al. (2009) An unrecognized extracellular function for an intracellular adapter protein released from the cytoplasm into the tumor microenvironment. *Proc Natl Acad Sci USA* 106(7):2182–2187.
28. Hirsch LR, et al. (2003) Nanoshell-mediated near-infrared thermal therapy of tumors under magnetic resonance guidance. *Proc Natl Acad Sci USA* 100(23):13549–13554.
29. Koay EJ, et al. (2014) Transport properties of pancreatic cancer describe gemcitabine delivery and response. *J Clin Invest* 124(4):1525–1536.
30. Pascal J, et al. (2013) Mechanistic modeling identifies drug-uptake history as predictor of tumor drug resistance and nano-carrier-mediated response. *ACS Nano* 7(12):11174–11182.
31. Pascal J, et al. (2013) Mechanistic patient-specific predictive correlation of tumor drug response with microenvironment and perfusion measurements. *Proc Natl Acad Sci USA* 110(35):14266–14271.
32. Sinek JP, et al. (2009) Predicting drug pharmacokinetics and effect in vascularized tumors using computer simulation. *J Math Biol* 58(4-5):485–510.
33. Ashley CE, et al. (2012) Delivery of small interfering RNA by peptide-targeted mesoporous silica nanoparticle-supported lipid bilayers. *ACS Nano* 6(3):2174–2188.
34. Epler K, et al. (2012) Delivery of ricin toxin a-chain by peptide-targeted mesoporous silica nanoparticle-supported lipid bilayers. *Adv Healthc Mater* 1(3):348–353.
35. Ashley CE, et al. (2011) The targeted delivery of multicomponent cargos to cancer cells by nanoporous particle-supported lipid bilayers. *Nat Mater* 10(5):389–397.
36. Mandelin J, et al. (2015) Selection and identification of ligand peptides targeting a model of castrate-resistant osteogenic prostate cancer and their receptors. *Proc Natl Acad Sci USA* 112(12):3776–3781.